

MIT Open Access Articles

*Coupled dynamics of flow, microstructure,
and conductivity in sheared suspensions*

The MIT Faculty has made this article openly available. **Please share**
how this access benefits you. Your story matters.

Citation: Olsen, Tyler, Ahmed Helal, Gareth H. McKinley, and Ken Kamrin. "Coupled Dynamics of Flow, Microstructure, and Conductivity in Sheared Suspensions." *Soft Matter* 12, no. 36 (2016): 7688–7697.

As Published: <http://dx.doi.org/10.1039/c6sm01199c>

Publisher: Royal Society of Chemistry

Persistent URL: <http://hdl.handle.net/1721.1/107240>

Version: Final published version: final published article, as it appeared in a journal, conference proceedings, or other formally published context

Terms of use: Creative Commons Attribution-NonCommercial 3.0 Unported





Cite this: *Soft Matter*, 2016,
12, 7688

Received 24th May 2016,
Accepted 3rd August 2016

DOI: 10.1039/c6sm01199c

www.rsc.org/softmatter

Coupled dynamics of flow, microstructure, and conductivity in sheared suspensions

Tyler Olsen, Ahmed Helal, Gareth H. McKinley and Ken Kamrin*

We propose a model for the evolution of the conductivity tensor for a flowing suspension of electrically conductive particles. We use discrete particle numerical simulations together with a continuum physical framework to construct an evolution law for the suspension microstructure during flow. This model is then coupled with a relationship between the microstructure and the electrical conductivity tensor. Certain parameters of the joint model are fit experimentally using rheo-electrical conductivity measurements of carbon black suspensions under flow over a range of shear rates. The model is applied to the case of steady shearing as well as time-varying conductivity of unsteady flow experiments. We find that the model prediction agrees closely with the measured experimental data in all cases.

Introduction

Microstructural anisotropy has been an active area of research for decades. It plays a critical role in biomechanics,^{5,7} plasticity,⁹ granular materials,^{3,6,26,32,37,41,45} liquid crystals,⁴⁴ and more. Some materials, such as elastic composites, have fixed anisotropy that does not evolve over time. However, other materials may develop anisotropy due to deformation, *e.g.* kinematic hardening of solids,⁹ or due to an externally-applied field, such as an electric field, as is typical of liquid crystals.⁴⁴

Of particular interest in this study is the flow-induced anisotropy of colloidal suspensions.^{11,12,22,28,31,34–36,40,46,47} Suspensions of carbon black, an electrically-conductive form of carbon, have recently found application in a class of semi-solid batteries called “flow batteries”.^{8,50} At concentrations above the percolation threshold, the carbon black creates an electrically conductive network inside the flowing electrolytes of the battery, allowing for higher reaction rates and overall system efficiency. However, it has been experimentally demonstrated that the networks in these carbon suspensions are highly sensitive to shearing.^{1,2,4,42} In these studies, the conductivity of the carbon network drops precipitously with shear and recovers dynamically when brought to rest. This has serious implications for battery performance if the evolution of network structure and conductivity are not properly considered during design. Recent studies⁴³ on optimizing the efficiency of a flow battery have neglected the effect of a shear-induced drop in suspension conductivity. In addition to the drop in conductivity, it has been observed that the suspension microstructure becomes anisotropic during shearing flow, which can lead to

anisotropic conductivity.^{18,29,49} In this study, we use discrete-particle simulations and continuum physical arguments to derive a general constitutive law for the flow-induced evolution of a tensor-valued measure of suspension network anisotropy. We couple this with a nonlinear structure–conductivity relation and show that the calibrated joint model makes quantitative predictions of conductivity evolution in many different experimental flows of carbon black.

We use a fabric tensor to describe the structure of the particle network in suspension. This concept was originally devised to describe the contact network in granular materials.^{26,32,41} The fabric tensor can be defined at the particle level with the relation

$$\mathbf{A}^P = \sum_{i=1}^{N_{\text{contacts}}} \mathbf{n}^{(i)} \otimes \mathbf{n}^{(i)} \quad (1)$$

where \otimes denotes the dyadic product and $\mathbf{n}^{(i)}$ the contact unit normals. The fabric tensor is a local (particle-level) 2nd-order tensor measure of the number and orientations of contacts with neighboring particles. The contact vectors in (1) are illustrated in Fig. 1.

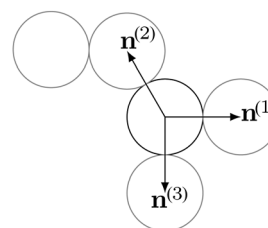


Fig. 1 Schematic of particles in contact showing unit contact normal vectors \mathbf{n}_i for computation of the fabric tensor.

Department of Mechanical Engineering, MIT, Cambridge, MA, USA.
E-mail: kkamrin@mit.edu



It is often illustrative to examine the average fabric of a group of particles rather than the particle-level information, *i.e.* $\mathbf{A} = \langle \mathbf{A}^p \rangle_p$. This definition yields a number of useful properties. The trace of \mathbf{A}^p is equal to the coordination number of contacts on a particle. Consequently, $\text{tr}\mathbf{A}$ represents the average coordination number, Z , of a group of particles. Second, this definition results in a symmetric, positive semi-definite tensor. This is appealing because these tensorial properties are shared by the conductivity tensor \mathbf{K} .

In a previous numerical study,³³ we modeled the conductivity tensor of a general particle network as a function of the average fabric tensor \mathbf{A} , by assuming the electrical properties of the network could be represented by a regular lattice of identical particles arranged to achieve with the same average fabric tensor as the given network. The fabric–lattice relationship can be inverted to obtain a model for conductivity as shown below in 3D:

$$\mathbf{K} = k_1 \frac{(\text{tr}\mathbf{A} - 2)^2}{\det \mathbf{A}} \mathbf{A} \quad \text{for } \text{tr}\mathbf{A} > 2, \quad 0 \text{ otherwise.} \quad (2)$$

The model was derived assuming that the suspending medium is a perfect insulator, the particles are perfect conductors, and that electrical resistance arises at the contacts between particles. Although the model neglects conductivity below the $\text{tr}\mathbf{A} = 2$ threshold—which occurs in particle assemblies with many disconnected islands and a small number of percolating chains—the model's predictions for both the isotropic and anisotropic components of conductivity are demonstrably stronger, over a wide range of coordination numbers, compared to the existing upper-bound models for particle-network conductivity,¹⁹ which ultimately relate to the Hashin–Shtrickman bounds.

Eqn (2) was validated for computer-generated random sphere networks, but was never tested experimentally; a byproduct of its usage in the current study is a *de facto* experimental test and a check on its robustness for non-spherical particles.

General evolution law

We set out to develop a continuum model to accurately characterize the evolution of flowing particle networks indicated by the aforementioned experiments. Although the fundamental quantity—the particle network—is composed of discrete units, we make a continuum approximation such that quantities at a point represent local spatial averages, *e.g.* velocity or fabric. This is a valid approximation since typical applications of these particle networks are several orders of magnitude larger than the constituents of the networks.

We define the velocity gradient $\mathbf{L} = \frac{\partial \mathbf{v}}{\partial \mathbf{x}}$, the strain-rate tensor $\mathbf{D} = \frac{1}{2}(\mathbf{L} + \mathbf{L}^T)$, and the spin tensor $\mathbf{W} = \frac{1}{2}(\mathbf{L} - \mathbf{L}^T)$. We postulate a fabric evolution law of the form $\dot{\mathbf{A}} = \Psi(\mathbf{A}, \mathbf{L})$, where $\dot{\mathbf{A}}$ denotes the material time derivative of \mathbf{A} . In order for an evolution law such as this to be indifferent under a change in an observer's frame of reference, the evolution law must be expressible as $\dot{\mathbf{A}} = \mathbf{W}\mathbf{A} - \mathbf{A}\mathbf{W} + \hat{\Psi}(\mathbf{A}, \mathbf{D})$, where $\hat{\Psi}$ is an isotropic function of the

fabric tensor and the strain-rate tensor.¹⁴ A representation theorem for isotropic functions of 3×3 symmetric tensors³⁸ can be applied, allowing us to write

$$\begin{aligned} \dot{\mathbf{A}} + \mathbf{A}\mathbf{W} - \mathbf{W}\mathbf{A} = & c_1 \mathbf{1} + c_2 \mathbf{A} + c_3 \mathbf{D} + c_4 \mathbf{A}^2 + c_5 \mathbf{D}^2 + c_6 (\mathbf{A}\mathbf{D} + \mathbf{D}\mathbf{A}) \\ & + c_7 (\mathbf{A}^2 \mathbf{D} + \mathbf{D}\mathbf{A}^2) + c_8 (\mathbf{A}\mathbf{D}^2 + \mathbf{D}^2 \mathbf{A}) + c_9 (\mathbf{A}^2 \mathbf{D}^2 + \mathbf{D}^2 \mathbf{A}^2) \end{aligned} \quad (3)$$

In the above expression, $c_i = c_i(\mathcal{I}_{\mathbf{A}, \mathbf{D}})$, where the full set of simultaneous invariants of \mathbf{A} and \mathbf{D} is

$$\mathcal{I}_{\mathbf{A}, \mathbf{D}} = \begin{cases} \text{tr}\mathbf{A}, & \text{tr}\mathbf{A}^2, & \text{tr}\mathbf{A}^3 \\ \text{tr}\mathbf{D}, & \text{tr}\mathbf{D}^2, & \text{tr}\mathbf{D}^3 \\ \text{tr}\mathbf{A}\mathbf{D}, & \text{tr}\mathbf{A}^2 \mathbf{D}, & \text{tr}\mathbf{A}\mathbf{D}^2, & \text{tr}\mathbf{A}^2 \mathbf{D}^2 \end{cases} \quad (4)$$

The left-hand side of (3) is the co-rotational time derivative of \mathbf{A} , or Jaumann rate, given the symbol $\dot{\mathbf{A}}$. In general, the left-hand side can be any objective time derivative of the tensor field, all of which are specializations of the Lie derivative.²⁴ Without loss of generality, we chose to use the co-rotational rate of \mathbf{A} for ease of modeling; other objective rates, such as the contravariant or covariant time derivatives, do not equal $\dot{\mathbf{A}}$ in a spin-free flow.¹³

The general evolution law in (3) has a large number of scalar functions that must be specified. For simplicity, we neglect higher-order tensorial terms by setting $c_i(\mathcal{I}_{\mathbf{A}, \mathbf{D}}) \equiv 0$ for $i \geq 4$. This leaves the quasi-linear form

$$\dot{\mathbf{A}} = c_1 \mathbf{1} + c_2 \mathbf{A} + c_3 \mathbf{D}. \quad (5)$$

The task of modeling, therefore, is reduced to choosing physically meaningful functions for c_1 , c_2 , and c_3 .

By examining the effect of each term on the evolution of the fabric, some physical constraints must be satisfied by the choice of the c_i . First, the fabric will be positive, isotropic, and unchanging after a long period of no flow; anisotropy induced by shearing flow must relax away over time once flow is stopped. This implies

$$c_1(\mathcal{I}_{\mathbf{A}, \mathbf{D}}) > 0; \quad c_2(\mathcal{I}_{\mathbf{A}, \mathbf{D}}) < 0 \quad \forall \mathbf{A}, \mathbf{D}. \quad (6)$$

If either of these constraints are violated, then the fabric would either decay away to a non-positive isotropic state or diverge.

Second, contacts are formed on the compressive axis of shearing flow and broken on the extension axis (as experimentally confirmed in Hoekstra *et al.*¹⁸). This gives us the condition

$$c_3(\mathcal{I}_{\mathbf{A}, \mathbf{D}}) < 0 \quad \forall \mathbf{A}, \mathbf{D}. \quad (7)$$

Third, while the electrical conductivity decreases with increasing shear rate, the conductivity never reaches zero despite the fluid being a strong insulator.² Based on the conductivity model assumption in (2), this implies that $\text{tr}\mathbf{A}$ remains above 2 at all times. This condition implies

$$-\frac{c_1}{c_2} > \frac{2}{3} \quad \forall \mathbf{A}, \mathbf{D}. \quad (8)$$



Finally, as the fabric is necessarily positive semi-definite, the evolution law must guarantee this property is preserved. A sufficient condition for this, as derived in the Appendix, is

$$\frac{c_1}{c_3} \leq -\sqrt{\frac{2}{3}}|\mathbf{D}|. \quad (9)$$

Numerical experiments

To gain insight on the relaxation behavior of the fabric, as characterized through the functions c_1 and c_2 , we created a discrete particle aggregation code. In our simulation, 100 000 particles are seeded into a periodic box at a 3.5% volume fraction and allowed to diffuse. The volume fraction was chosen to match approximately the volume fraction in physical experiments that will be described in subsequent sections. Particles and clusters are assigned velocities such that the distance that a cluster moves in a single time step is drawn from a Gaussian distribution with variance $D\Delta t$, where D is the diffusion coefficient, and Δt is the simulation time step length. As hit-and-stick behavior is typical in diffusion-limited aggregation,²¹ all clusters in contact after a step are deemed to stick, creating a larger cluster. As clusters grow, the diffusion coefficient is adjusted according to $D = D_0/N$, where D_0 is the diffusion coefficient for a single particle, and N is the number of particles in a cluster. Because clusters typically have a snake-like shape, dominated by long strands of particles, this relation was chosen for its similarity to the asymptotic solution for the diffusion coefficient of a string of N particles.¹⁵ We neglect hydrodynamic forces between clusters and rotational diffusion. These assumptions result in a code similar to the off-lattice Monte Carlo aggregation method described in Rotureau *et al.* 2004.³⁹ The effect of shear thickening was not considered, since the method represents particles in a quiescent medium subjected to Brownian forces.

The simulation results are shown in Fig. 2, where \mathbf{A}_{ss} is the steady-state fabric. After a brief startup period, the deviation of the average coordination number from steady state ($\text{tr}\mathbf{A}_{ss} - \text{tr}\mathbf{A}$) is related to time through a power law

$$(\text{tr}\mathbf{A}_{ss} - \text{tr}\mathbf{A}) \sim (t/\Delta t)^{-0.745} \quad (10)$$

Although many studies, both experimental²³ and numerical,³⁹ have examined the evolution of various cluster properties, such as radius of gyration and mass, very few have examined the average coordination of particles. We have not found any prior studies that track the average coordination number through time, though it seems plausible that this power law exponent could be deduced through a random walk analysis.

Form of evolution coefficients

Motivated by the power-law decay of $\text{tr}\mathbf{A}$ to steady state that we have just determined, we choose the following functional forms for the c_i coefficients:

$$c_1 = \frac{1}{3} \left(\frac{Z_0}{\tau} (Z_0 - \text{tr}\mathbf{A})^n + \beta Z_\infty |\mathbf{D}| \right) \quad (11)$$

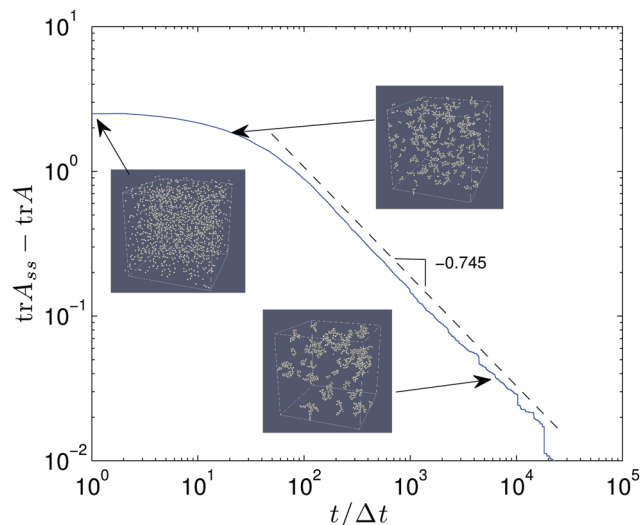


Fig. 2 Log-log plot of $\text{tr}\mathbf{A}_{ss} - \text{tr}\mathbf{A}$ vs. time shows power-law evolution of $\text{tr}\mathbf{A}$ to steady state in the absence of external shearing. Inset images (for illustration purposes only) from a highly dilute simulation demonstrate the aggregation of particles into clusters in the simplified discrete model. Clusters in the simulation used to generate the curve span the domain after a short period of aggregation, forming conductive networks.

$$c_2 = -\left(\frac{1}{\tau} (Z_0 - \text{tr}\mathbf{A})^n + \beta |\mathbf{D}| \right) \quad (12)$$

$$c_3 = \alpha \quad (13)$$

where $Z_0 = \text{tr}\mathbf{A}_{ss}$ (in the absence of flow), $Z_\infty = \text{tr}\mathbf{A}_{ss}$ as $|\mathbf{D}| \rightarrow \infty$, τ is the time scale of thermal fabric relaxation, β reflects the network creation or disruption due to non-affine flow perturbations, α is the initial rate of anisotropy formation when started from an isotropic state, and n characterizes the power-law relaxation to the no-flow steady state (see Fig. 2). The particular forms of the functions were chosen in order to satisfy all of the constraints (6–9) and to reproduce the power-law relaxation of the coordination number observed in Fig. 2. The above constraints imply the following inequalities on these parameters:

$$Z_0, Z_\infty > 2 \quad (14)$$

$$\tau, \beta > 0 > \sqrt{2/3} \alpha > -\beta Z_\infty / 3 \quad (15)$$

The value of n can be predicted from the discrete simulation data by taking the trace of eqn (5), setting \mathbf{L} to 0, integrating to find $\text{tr}\mathbf{A}$ as a function of time, and relating the answer back to the power-law in eqn (10). Using this, we find $n = 1.34$.

In previous studies on attractive colloids, both experiments²⁰ and numerical simulations²⁵ indicate that the average coordination number at rest is slightly above the isostatic condition of frictionless, hard spheres ($Z = 6$) for certain degrees of attraction. In our experiments, the carbon black of interest has an attractive interaction potential of $12k_B T$,⁴⁸ which is similar to the materials studied in the aforementioned studies. Thus, for consistency, we expect Z_0 to be ≈ 7 for our material.



Experimental methods

The system studied is a carbon black suspension prepared in the absence of any dispersant by mixing carbon black powder (Cabot Vulcan XC72R of specific gravity 1.8) in a light mineral oil (Sigma-Aldrich, specific gravity 0.838, viscosity 20 mPa s) as described in ref. 12 at a weight concentration of 8% w/w (approximately 3.5% volume fraction). The suspension is sonicated for one hour and mixed vigorously prior to each test to minimize the effects of sedimentation.

Simultaneous rheo-electric measurements were performed using a custom setup on an ARG2 torsional stress-controlled rheometer with a parallel plate geometry. This setup uses liquid metal (EGaIn) to create a low-friction continuous electrical connection to the rotating shaft,¹⁶ allowing a prescribed voltage to be applied across the shearing suspension layer. DC potentiostatic tests with $\phi = 100$ mV were performed using a Solartron SI1287 potentiostat. The plates (diameter $d = 40$ mm, average surface roughness $R_a = 0.10$ μm), acting as a two-electrode system, are coated with gold to reduce contact resistance. All rheo-electric tests were performed at gap $h = 0.75$ mm and $T = 26 \pm 0.3$ °C. A schematic of the device used to perform the rheo-electric measurements is shown in Fig. 3.

Two sets of experiments were performed using the setup described above. The first was a set of steady-state current measurements taken at nominal shear rates in the range $\dot{\Gamma} = \omega R/h \in [0, 300]$ s⁻¹. At each shear rate, both the current and stress were allowed to equilibrate before the measurement was recorded to ensure that it had relaxed to its steady value. The shear rates were swept in descending order to mitigate complications such as shear-induced phase separation that arise at low shear rates, below $\dot{\Gamma} \sim 20$ s⁻¹.¹⁶

The second dataset was a collection of transient ramp tests wherein current data was collected continuously for the duration of the test. The ramp tests consisted of 5 minutes of nominal shear rate $\dot{\Gamma} = \dot{\Gamma}_1$, ramping linearly to $\dot{\Gamma}_2$ over duration t_R , holding for 5 minutes, and abruptly setting $\dot{\Gamma} = 0$, collecting data for 15 additional minutes. Pre-shear at $\dot{\Gamma} = 100$ s⁻¹ was applied for 5 minutes before each test to ensure consistent initial conditions.

The parameters Z_∞ , β , and α were fitted to the steady-state current measurements using the `fminunc` Matlab optimization routine, minimizing the squared difference between predicted and measured electrical currents. The τ parameter, which is primarily responsible for controlling the fabric's relaxation time, was chosen from the experimental dynamics of the ramp tests. Lastly, the k_1 parameter can be chosen to match the steady-state current observed at $\dot{\Gamma} = 0$.

The predicted current is calculated by evaluating the integral

$$I(t) = 2\pi \int_0^R K_{zz}(\mathbf{A}(r, t)) \cdot \frac{\phi}{h} r dr \quad (16)$$

where K_{zz} is the component of conductivity perpendicular to the plate, ϕ is the applied potential difference across the plates, h is the plate separation, and R is the plate radius. Note that the fabric tensor is a function of radial position; each point along a radius is subjected

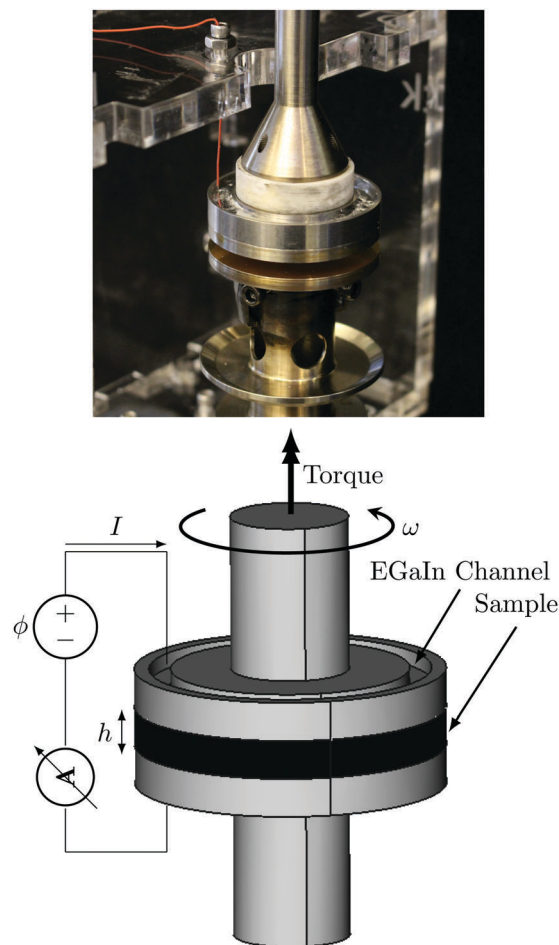


Fig. 3 (top) Photo of device used to perform simultaneous rheo-electric measurements. (bottom) Circuit diagram of experimental setup.

to a different shear rate due to the applied torsional motion, and thus evolves differently. The form of (16) can be modified slightly in order to solve for the current at steady-state for a given nominal shear rate $\dot{\Gamma}$, by substituting $\mathbf{A}(r, t)$ with $\mathbf{A}_{ss}(\dot{\gamma} = \dot{\Gamma}r/R)$ where $\mathbf{A}_{ss}(\dot{\gamma})$ is the steady-state fabric tensor, whose components are obtained algebraically from eqn (5) by defining \mathbf{D} and \mathbf{W} to correspond to simple shearing at $\dot{\gamma}$ and setting $\dot{\mathbf{A}} = 0$. A detailed outline of the fitting procedure can be found in the Appendix.

To simulate the electrical current for a transient test, the evolution law must be directly integrated at each point across the disk where the conductivity will be evaluated. To do this, one must input the time-dependent nominal shear-rate $\dot{\Gamma}(t)$ from the experimental protocol. The evolution law was numerically integrated to obtain the fabric tensor at all time points. After the fabric is known, (16) can be approximated directly using a Riemann sum to give the predicted current as a function of time.

Results

The power law index n was determined *a priori* using the discrete simulation, and all other model parameters were found using the fitting procedure described above. The parameters used to



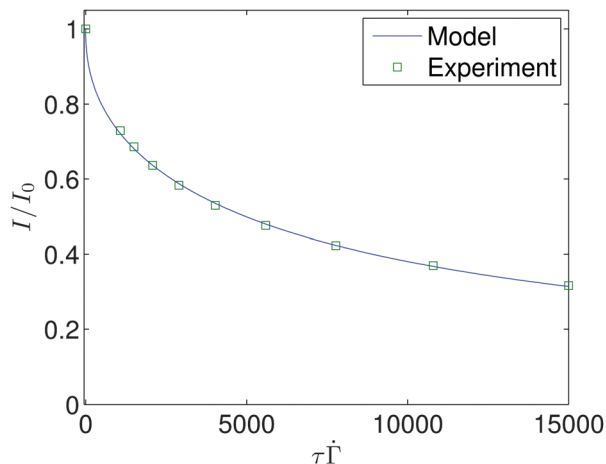


Fig. 4 Model fit of steady-state current measurements at different nominal shear rates. Values are normalized by the static current measurement I_0 .

generate all of the following plots, which satisfy all necessary constraints, are $Z_0 = 7$, $Z_\infty = 2.41$, $\tau = 50$ s, $\beta = 0.009$, $\alpha = -0.0089$, $n = 1.34$, and $k_1 = 0.0282$ S m $^{-1}$.

Steady-state experiments

Fig. 4 shows the steady-state current predicted by the model compared to experimental data measured at various nominal shear rates, represented in the form of a scaled current as a function of a dimensionless shear rate, or Deborah number. The results indicate the model does an excellent job predicting the steady-state current measurements over the entire tested range of $\dot{\Gamma}$.

Transient ramp experiments

The results in Fig. 5 show the temporal evolution of the current under imposed shearing normalized by the static current measurement. The close agreement indicates that the model is capable of making accurate, quantitative predictions for the transient behavior of the normalized current. The close agreement at the steady plateaus of $\dot{\Gamma}_1$ and $\dot{\Gamma}_2$ were expected due to the close fit of steady-state data in Fig. 4. The most critical test in the ramp experiments was the relaxation of the conductivity when flow was abruptly stopped. The model does an excellent job predicting this non-trivial behavior, especially given that each point along the radius of the plate begins decaying from a different initial steady-state condition.

Asymptotic model predictions

With the model, we were able to examine analytical solutions for the evolution of the coordination number Z in the limiting cases of diffusion-dominated and shear-dominated evolution. The evolution of Z is governed by the differential equation that results from taking the trace of (5) under the assumption of incompressible flow, substituting (11) and (12) into the resulting expression, and collecting terms:

$$\dot{Z} = \frac{1}{\tau}(Z_0 - Z)^{n+1} + \beta|\mathbf{D}|(Z_\infty - Z) \quad (17)$$

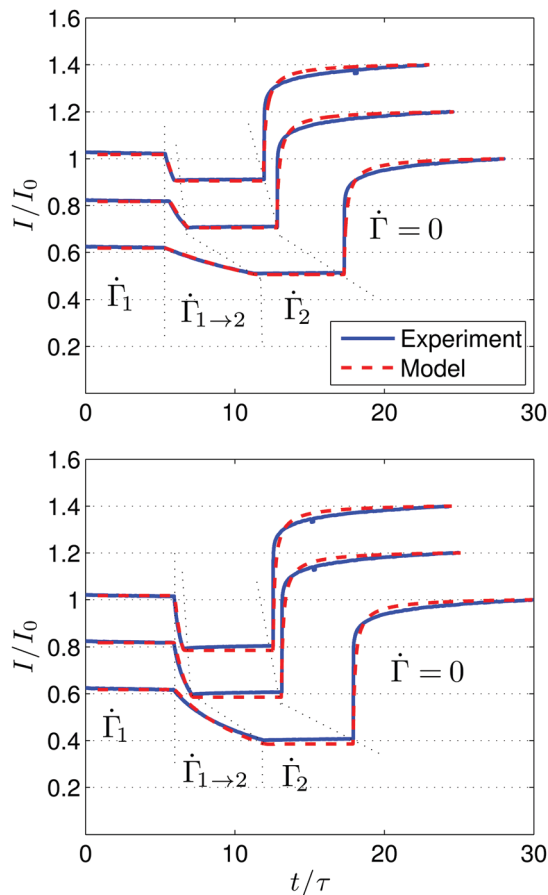


Fig. 5 Transient ramp experiments from (top) $\tau \dot{\Gamma}_1 = 2500$ to $\tau \dot{\Gamma}_2 = 5000$, and (bottom) $\tau \dot{\Gamma}_1 = 2500$ to $\tau \dot{\Gamma}_2 = 10000$ with ramp times t_R/τ of 0.6, 1.2, and 6 (top to bottom). A vertical offset of 0.2 has been added between successive curves for clarity, with the y-axis correct as displayed for the bottom curve. Current values are normalized by the static current measurement I_0 .

The case of diffusion-dominated evolution corresponds to the condition $|\mathbf{D}| \rightarrow 0$. Applying this to (17) results in an ODE that, together with an appropriate initial condition, may be analytically solved for $Z(t)$. The solution of this ODE predicts a power-law approach of Z to Z_0 given by $|Z - Z_0| \sim t^{-1/n}$. Shear-dominated evolution is given by the condition $|\mathbf{D}| \gg 1/(\beta\tau)$. Under these conditions, the first term in (17) is much smaller than the second, and the resulting ODE predicts exponential decay of Z to Z_∞ , given by $Z - Z_\infty \sim e^{-\beta|\mathbf{D}|t}$. These two analytical results highlight the important transition from power-law to exponential evolution as $|\mathbf{D}|$ increases. The power-law behavior at low shear is consistent with our numerical simulations of particle aggregation and the $|\mathbf{D}| = 0$ dynamics in our experiments, shown in Fig. 5. The exponential decay is consistent with previously published simulations of attractive fluid-particle systems in shear-dominated flow.²⁵

These analytical results are plotted in Fig. 6 together with numerically integrated solutions of (17). In all cases, the initial condition was set to $Z|_{t=0} = (Z_0 + Z_\infty)/2$. Each panel shows the same numerically-integrated data (solid lines), with the only difference between the top and bottom being the axes definitions.



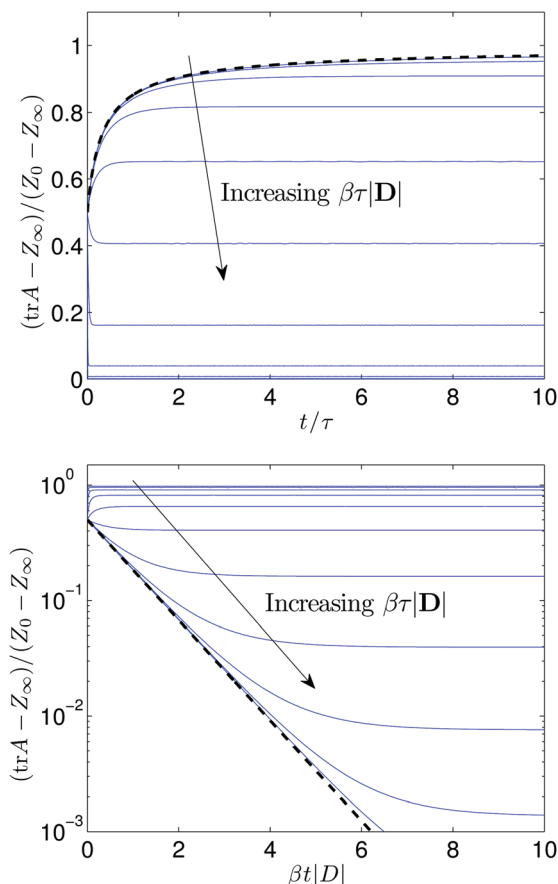


Fig. 6 Evolution of $Z = \text{tr}\mathbf{A}$ in pure shearing under different shear rates, as predicted by the model. (top) $\beta\tau|\mathbf{D}| \ll 1$ yields power-law approach of Z to steady state; $|Z - Z_0| \sim t^{-1/n}$ as $|\mathbf{D}| \rightarrow 0$, dotted line. (bottom) $\beta\tau|\mathbf{D}| \gg 1$ yields exponential approach to steady state; $\log(Z - Z_\infty) \sim -|\mathbf{D}|t$ as $|\mathbf{D}| \rightarrow \infty$, dotted line.

On the top and bottom, respectively, the thick dashed line is the analytical solution at $|\mathbf{D}| = 0$ and the analytical solution for shear-dominated flow, both defined above.

Discussion

We have demonstrated a model for the conductivity of sheared suspensions by linking conductivity and flow to a common microstructural description. Although the model parameters were obtained using conductivity measurements, it is interesting to note the following points, which emphasize that the structure indeed plays the assumed role: (i) the best-fit parameters obtained from the experiments obey constraints expected of a particle structure (eqn (6)–(9)), (ii) parameters taken from existing particle-level simulation data— n and Z_0 —yield quantitatively accurate results (Fig. 4 and 5) when used in the evolution law, and (iii) the structural evolution model, on which the experimental agreement hinges, gives the same asymptotic behaviors as those observed in suspension simulations. Conversely, our approach highlights the possibility of using conductivity measurements to infer discrete microstructural properties of systems, a notion also suggested in ref. 51. It should be noted that a simpler constitutive specialization

of the c_i functions using $n = 0$ does not capture the measured evolution of conductivity well. A model using $n = 0$ predicts exponential, rather than power-law, relaxation of fabric upon cessation of flow. The resulting conductivity evolution cannot predict the observed behavior shown in Fig. 5. For comparison, we show the predictions of such a model (using $n = 0$) in the Appendix.

There are strong analogies to be drawn between this proposed microstructural evolution model coupled to conductivity, and the thixotropic family of rheological models. In thixotropy models, fluid viscosity is often modeled as a function of an implicit material field that is intended to represent the underlying fluid microstructure. This field is prescribed to evolve according to a differential equation, properly stated as a transport equation that encompasses both the advective conservation and the non-conservative creation and destruction of the field.^{27,30} It should be unsurprising that our conductivity model strongly resembles these thixotropy models, as the fluid microstructure is believed to give rise to the flow-history-dependent behavior of both the conductivity and viscosity in these types of complex fluids. See the Appendix for a demonstration of some conductivity modeling results that mirror those often associated with thixotropy.

The new model (eqn (2), (5) and (11–13)) can be applied as a quantitative tool for designing systems of flowing, electrically-active particulate suspensions, for example in a semi-solid flow battery architecture.^{8,17,43} Because the shear-induced conductivity loss can be strong even under moderate shear rates, the ability to predict this component of the performance envelope through a quantitative continuum model should enable subsequent geometric and flow protocol optimization.

Appendix

Constraint derivations

This section lays out in more detail the derivation of constraints on the fabric tensor evolution law below:

$$\dot{\mathbf{A}} = c_1 \mathbf{1} + c_2 \mathbf{A} + c_3 \mathbf{D}. \quad (\text{A1})$$

Trace condition. To find the physical conditions on the coefficients in the evolution law, we take the trace of (A1) and solve for the steady-state trace of the fabric, $\text{tr}\mathbf{A}_{\text{ss}}$. The flow is assumed to be incompressible, so $\text{tr}\mathbf{D} = 0$. We observe experimentally that electrical conductivity never entirely shuts off, regardless of the imposed strain rate $|\mathbf{D}|$. According to (2) in the main text, this implies that $\text{tr}\mathbf{A} > 2$. This restriction yields a constraint between c_1 and c_2 .

$$0 = 3c_1 + c_2 \text{tr}\mathbf{A}_{\text{ss}} \quad (\text{A2})$$

$$\text{tr}\mathbf{A}_{\text{ss}} = -\frac{3c_1}{c_2} > 2 \quad (\text{A3})$$

Positive semidefinite constraint. The fabric tensor is by definition a symmetric, positive semi-definite tensor. Thus, we must ensure that under no circumstances will the evolution law violate this condition. We can write the fabric tensor as

$$\mathbf{A} = \mathbf{Q}\mathbf{A}\mathbf{Q}^T \quad (\text{A4})$$



where \mathbf{Q} is the eigenvector matrix and $\mathbf{\Lambda}$ is a diagonal matrix of eigenvalues. The time derivative of this quantity, then, is

$$\dot{\mathbf{A}} = \mathbf{Q}\dot{\mathbf{\Lambda}}\mathbf{Q}^T + \dot{\mathbf{Q}}\mathbf{\Lambda}\mathbf{Q}^T + \mathbf{Q}\mathbf{\Lambda}\dot{\mathbf{Q}}^T \quad (\text{A5})$$

This can be rewritten as

$$\dot{\mathbf{A}} = \mathbf{Q}\dot{\mathbf{\Lambda}}\mathbf{Q}^T + \mathbf{\Lambda}\mathbf{\Omega} - \mathbf{\Omega}\mathbf{\Lambda} \quad (\text{A6})$$

where $\mathbf{\Omega} = \dot{\mathbf{Q}}\mathbf{Q}^T$, the spin of the eigenvectors, is a skew-symmetric matrix.

Suppose that during flow one of the eigenvalues approaches zero. The condition that \mathbf{A} always be positive semi-definite requires that the rate of change of that eigenvalue be greater than or equal to zero. Without loss of generality, we choose $\Lambda_{11} = \lambda_1$, to be zero. Suppose also that our global basis was chosen such that, at the moment when $\lambda_1 = 0$, the eigenvectors were aligned with the global basis, so $\mathbf{Q} = \mathbf{1}$. The evolution for the λ_1 eigenvalue is

$$\dot{\lambda}_1 = c_1 + c_3 D_{11} \geq 0 \quad (\text{A7})$$

Now, due to our constraint from (7) in the main text, we know that c_3 is a negative-valued function, so we rewrite it as

$$\dot{\lambda}_1 = c_1 - \hat{c}_3 D_{11} \geq 0 \quad (\text{A8})$$

where $\hat{c}_3 = -c_3$ is a positive-valued function.

It can be shown that for incompressible flow, $|\mathbf{D}| \geq \sqrt{\frac{3}{2}}|D_{11}|$. Therefore it is sufficient to find a relationship between c_1 and \hat{c}_3 that satisfies

$$c_1 - \hat{c}_3 \sqrt{\frac{2}{3}}|\mathbf{D}| \geq 0 \quad (\text{A9})$$

Solving, and substituting c_3 back in, we obtain the final form of the constraint.

$$\frac{c_1}{c_3} \leq -\sqrt{\frac{2}{3}}|\mathbf{D}| \quad (\text{A10})$$

Linearized evolution law

In the main text, we assert that the evolution law with the power-law index n set to 0 cannot capture the power-law relaxation behavior observed at low shear rates. The fabric relaxes at an exponential rate when $n = 0$, rather than at the power-law rate observed in our simulations. If we force fit $n = 0$ and refit the experimental data using the fitting procedure, we obtain the parameters $Z_0 = 8.8$, $Z_\infty = 3.2$, $\tau = 1/50 \text{ s}^{-1}$, $\beta = 0.002$, $\alpha = -0.0026$, $n = 0$, and $k_1 = 0.0241 \text{ S m}^{-1}$. The model is able to adequately reproduce the steady-state current measurements, but it fails to capture the relaxation upon cessation of flow. The results are shown in Fig. 7. Compare results to Fig. 5 in the main text.

Thixotropy

As discussed at the end of the main text, the evolution law coupled with the fabric–conductivity relationship (2) is analogous to the family of thixotropic rheological models. The defining feature of these models is that there is an observed variable, usually viscosity, described as a function of an internal variable that evolves in accord with some evolution rule. In these models, the internal variable typically represents some aspect of the

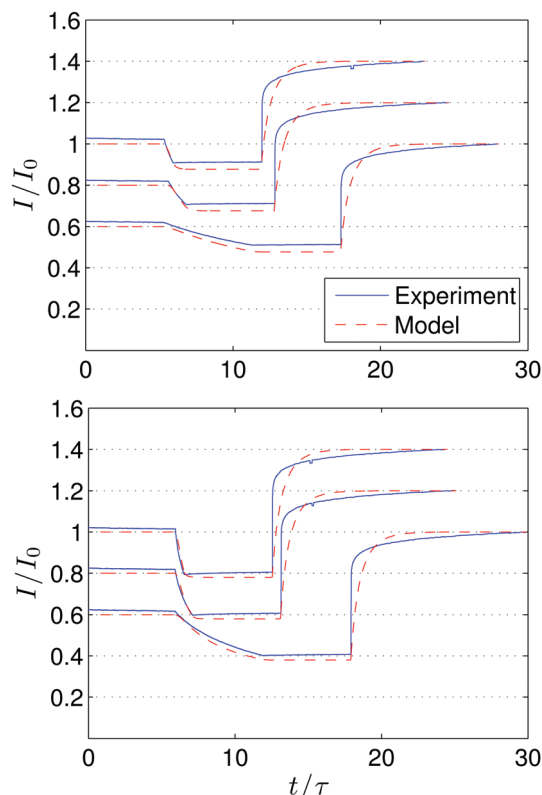


Fig. 7 Transient ramp experiments reproduced with the evolution law with $n = 0$. The model fails to adequately capture the relaxation behavior that occurs upon cessation of flow.

fluid microstructure. A more comprehensive definition and review of thixotropy models can be found in Mewis and Wagner.²⁷ In our study, the observed variable is the electrical conductivity and the implicit structural variable is the fabric tensor which evolves due to shearing flow and particle Brownian motion. As a result, the observed conductivity is dependent on the full history of flow; there is not a one-to-one relationship between conductivity and shear rate. The non-unique behavior can be inferred from Fig. 5, but can be seen clearly by re-plotting one of the ramp experiments as normalized current against the normalized nominal shear rate $\tau\dot{\Gamma}_0$, shown in Fig. 8. It can be seen, for example, that the conductivity takes multiple values at $\dot{\Gamma} = 0 \text{ s}^{-1}$.

A common characteristic of thixotropic material response is the formation of stable loops in the observed variable when subjected to cyclic input (e.g.: up/down ramps in shear rate). To demonstrate this phenomenon, we simulated a set of experiments where a simple shear rate is ramped linearly from $\dot{\Gamma} = 0 \text{ s}^{-1}$ to $\dot{\Gamma} = 5/(\beta\tau) \text{ s}^{-1}$ and back down again over the cycle period T . The maximum shear rate was chosen to be in the intermediate range of diffusion-dominated and shear-dominated rates. See the “Asymptotic Model Predictions” part of the Results section for more details. The input was cycled until the conductivity had reached a visually-stable trajectory. Six different cycle periods were chosen in order to probe the range of short cycle times ($T/\tau = 0.05$) to long cycle times ($T/\tau = 500$). The results of the simulation are shown in Fig. 9. For very short cycle times, we observe that the



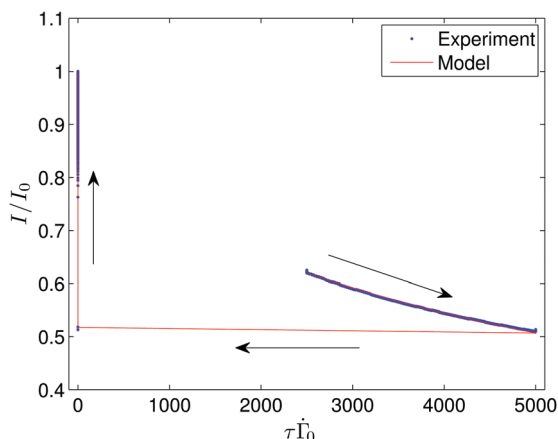


Fig. 8 Ramp experiment replotted from Fig. 5 show non-unique relationship between measured current and imposed shear rate. Arrows show progression of time.

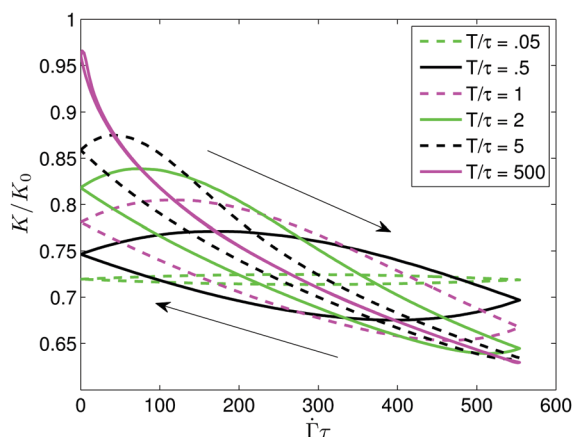


Fig. 9 Plot of normalized stable conductivity loops that are formed during cyclic shear rate simulations for six different cycle periods. Arrows indicate the progression of time along each side of the cycle.

driving force changes much faster than the conductivity can evolve, resulting in small oscillations around a single value of conductivity. For very long cycle times, we observe that the conductivity is able to essentially maintain its long-term steady-state value at all times, with small deviations occurring only at very low shear rates. Intermediate cycle times show the transition between the short and long cycle states. In these cases, the comparable time scales of the fabric evolution and the driving shear rate lead to the formation of large hysteresis loops in the conductivity trajectories.

A striking feature of the figure is the non-monotonic conductivity in the increasing shear rate portion of the stable loops. At low, increasing shear rates, the rate of fabric formation due to the random motion of particles is still greater than the rate of fabric destruction due to shearing up to some finite $\dot{\Gamma}$, where the rates are balanced and we observe a local maximum in conductivity. This non-monotonic effect is again observed at the high, decreasing range of shear rates, although the effect is less pronounced. This is evidenced by the local

minimum in the observed conductivity that does not correspond exactly with the maximum shear rate. Similar non-monotonic behavior in conductivity has been seen experimentally by Genz *et al.*¹⁰

Data-fitting algorithm

Algorithm 1 Computation of \mathbf{A}_{ss} for given simple-shear flow with strain-rate $\dot{\gamma}$

Input: Simple-shear strain-rate $\dot{\gamma}$.

Output: Steady-state fabric \mathbf{A}_{ss}

Construct $\mathbf{L} = \dot{\gamma} \hat{x} \otimes \hat{y}$.

Define $\mathbf{D} = \frac{1}{2}(\mathbf{L} + \mathbf{L}^T)$, $\mathbf{W} = \frac{1}{2}(\mathbf{L} - \mathbf{L}^T)$.

Solve nonlinear equation for $\text{tr}\mathbf{A}_{ss}$.

Compute c_1 and c_2 from $\text{tr}\mathbf{A}_{ss}$ and $|\mathbf{D}|$

Use algebraic solution of (A1) with $\dot{\mathbf{A}} = 0$ to find \mathbf{A}_{ss} .

To fit the model, we minimize the squared error between the model prediction and experimental values. The procedure for calculating this error is given in Algorithm 2.

Algorithm 2 Objective function for evolution law optimization routine

Input: $Z_0, Z_\infty, \tau, \beta, \alpha, n, k_1$

Output: Squared error = *Score*

Score $\leftarrow 0$

for all $\dot{\Gamma}_i \in \{\text{Experimental shear rates}\}$ **do**

 Compute $I_{ss}(\dot{\Gamma}_i)$ using (13) from main text
 and Algorithm 1

 Compute error between model and experiment:

$$err \leftarrow (I_{ss}(\dot{\Gamma}_i) - I_{exp}(\dot{\Gamma}_i))^2.$$

Score \leftarrow *Score* + *err*

end for

return *Score*

The following algorithm outlines the high-level procedure for fitting the evolution law to a set of experimental data. It relies heavily on the preceding procedures laid out in Algorithm 1 and Algorithm 2.

Algorithm 3 Experimental fitting procedure

Input: List of $\{\dot{\Gamma}, I_{exp}\}$ pairs from steady-state experiments

Output: Evolution law coefficients $\{Z_0, Z_\infty, \tau, \beta, \alpha, n\}$

Estimate b_1 from relaxation time of transient ramp tests.

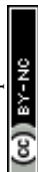
Choose n to match discrete particle simulations

Call *fminunc* with objective function given by Algorithm 2.

$\{Z_0, Z_\infty, \tau, \beta, \alpha, n\} \leftarrow$ Output from *fminunc*.

Verify that all constraints are satisfied

Adjust b_1 estimate and repeat until $\dot{\gamma}_0 = 0$ transient is well-matched.



Acknowledgements

The authors acknowledge support from the Joint Center for Energy Storage Research (JCESR), an Energy Innovation Hub funded by the U.S. Department of Energy, Office of Science, Basic Energy Science (BES). The authors declare that there are no conflicts of interest.

References

- 1 I. Alig, T. Skipa, M. Engel, D. Lellinger, S. Pegel and P. Pötschke, Electrical conductivity recovery in carbon nanotube–polymer composites after transient shear, *Phys. Status Solidi B*, 2007, **244**(11), 4223–4226.
- 2 T. Amari and K. Watanabe, Flow properties and electrical conductivity of carbon black–linseed oil suspension, *J. Rheol.*, 1990, **34**(2), 207.
- 3 E. Azéma, N. Estrada and F. Radjai, Nonlinear effects of particle shape angularity in sheared granular media, *Phys. Rev. E: Stat., Nonlinear, Soft Matter Phys.*, 2012, **86**(4), 041301.
- 4 W. Bauhofer, S. C. Schulz, A. E. Eken, T. Skipa, D. Lellinger, I. Alig, E. J. Tozzi and D. J. Klingenberg, Shear-controlled electrical conductivity of carbon nanotubes networks suspended in low and high molecular weight liquids, *Polymer*, 2010, **51**(22), 5024–5027.
- 5 J. E. Bischoff, E. M. Arruda and K. Grosh, A Microstructurally Based Orthotropic Hyperelastic Constitutive Law, *J. Appl. Mech.*, 2002, **69**(5), 570.
- 6 F. da Cruz, S. Emam, M. Prochnow, J.-N. Roux and F. Chevoir, Rheophysics of dense granular materials: discrete simulation of plane shear flows, *Phys. Rev. E: Stat., Nonlinear, Soft Matter Phys.*, 2005, **72**(2), 021309.
- 7 J. M. Deneweth, S. G. McLean and E. M. Arruda, Evaluation of hyperelastic models for the non-linear and non-uniform high strain-rate mechanics of tibial cartilage, *J. Biomech.*, 2013, **46**(10), 1604–1610.
- 8 M. Duduta, B. Ho, V. C. Wood, P. Limthongkul, V. E. Brunini, W. Craig Carter and Y.-M. Chiang, Semi-Solid Lithium Rechargeable Flow Battery, *Adv. Energy Mater.*, 2011, **1**(4), 511–516.
- 9 C. O. Frederick and P. J. Armstrong, A mathematical representation of the multiaxial Bauschinger effect, *Mater. High Temp.*, 2007, **24**(1), 1–26.
- 10 U. Genz, J. A. Helsen and J. Mewis, Dielectric spectroscopy of reversibly flocculated dispersions during flow, *J. Colloid Interface Sci.*, 1994, **165**(1), 212–220.
- 11 V. Grenard, N. Taberlet and S. Manneville, Shear-induced structuration of confined carbon black gels: steady-state features of vorticity-aligned flocs, *Soft Matter*, 2011, **7**(8), 3920–3928.
- 12 V. Grenard, T. Divoux, N. Taberlet and S. Manneville, Time-scales in creep and yielding of attractive gels, *Soft Matter*, 2014, **10**, 1555–1571.
- 13 M. E. Gurtin, E. Fried and L. Anand, *The Mechanics and Thermodynamics of Continua*, Cambridge University Press, 2010.
- 14 G. L. Hand, A theory of anisotropic fluids, *J. Fluid Mech.*, 1962, **13**(1), 33.
- 15 J. Happel and H. Brenner, *Low Reynolds number hydrodynamics: with special applications to particulate media*, Springer Science & Business Media, 2012, vol. 1.
- 16 A. Helal, T. Divoux and G. H. McKinley, Simultaneous rheo-electric measurements of strongly conductive complex fluids, 2016, *arXiv preprint arXiv:1604.00336*.
- 17 A. Helal, K. Smith, F. Fan, X. Wei Chen, J. Miguel Nobrega, Y.-M. Chiang and G. H. McKinley, Study of the rheology and wall slip of carbon black suspensions for semi-solid flow batteries, The Society of Rheology 86th Annual Meeting, 2014.
- 18 H. Hoekstra, J. Vermant, J. Mewis and G. G. Fuller, Flow-induced anisotropy and reversible aggregation in two-dimensional suspensions, *Langmuir*, 2003, 9134–9141.
- 19 A. Jagota and C. Y. Hui, The Effective Thermal Conductivity of a Packing of Spheres, *J. Appl. Mech.*, 1990, 789–791.
- 20 I. Jorjadze, L.-L. Pontani, K. A. Newhall and J. Brujić, Attractive emulsion droplets probe the phase diagram of jammed granular matter, *Proc. Natl. Acad. Sci. U. S. A.*, 2011, **108**(11), 4286–4291.
- 21 T. A. Witten Jr and L. M. Sander, Diffusion-limited aggregation, a kinetic critical phenomenon, *Phys. Rev. Lett.*, 1981, **47**(19), 1400–1402.
- 22 N. Koumakis, M. Laurati, S. U. Egelhaaf, J. F. Brady and G. Petekidis, Yielding of Hard-Sphere Glasses during Start-Up Shear, *Phys. Rev. Lett.*, 2012, **108**(9), 098303.
- 23 M. Y. Lin, H. M. Lindsay, D. A. Weitz, R. C. B. R. Klein, R. C. Ball and P. Meakin, Universal diffusion-limited colloid aggregation, *J. Phys.: Condens. Matter*, 1990, **2**(13), 3093.
- 24 J. E. Marsden and T. J. R. Hughes, *Mathematical foundations of elasticity*, Courier Corporation, 1994.
- 25 N. S. Martys, D. Lootens, W. George and P. Hébraud, Contact and stress anisotropies in start-up flow of colloidal suspensions, *Phys. Rev. E: Stat., Nonlinear, Soft Matter Phys.*, 2009, **80**(3), 031401.
- 26 M. M. Mehrabadi, S. Nemat-Nasser and M. Oda, On statistical description of stress and fabric in granular materials, *Int. J. Numer. Anal. Methods Geomech.*, 1982, **6**(1), 95–108.
- 27 J. Mewis and N. J. Wagner, Thixotropy, *Adv. Colloid Interface Sci.*, 2009, **147**, 214–227.
- 28 A. Mohraz and M. J. Solomon, Orientation and rupture of fractal colloidal gels during start-up of steady shear flow, *J. Rheol.*, 2005, **49**(3), 657–681.
- 29 J. F. Morris and B. Katyal, Microstructure from simulated Brownian suspension flows at large shear rate, *Phys. Fluids*, 2002, **14**(6), 1920.
- 30 A. Mujumdar, A. N. Beris and A. B. Metzner, Transient phenomena in thixotropic systems, *J. Non-Newtonian Fluid Mech.*, 2002, **102**(2), 157–178.
- 31 A. Singh Negi and C. O. Osuji, New insights on fumed colloidal rheology—shear thickening and vorticity-aligned structures in flocculating dispersions, *Rheol. Acta*, 2009, **48**(8), 871–881.
- 32 M. Oda, S. Nemat-Nasser and M. M. Mehrabadi, A statistical study of fabric in a random assembly of spherical granules, *Int. J. Numer. Anal. Methods Geomech.*, 1982, **6**, 77–94.



- 33 T. Olsen and K. Kamrin, Modeling tensorial conductivity of particle suspension networks, *Soft Matter*, 2015, **11**(19), 3875–3883.
- 34 C. O. Osuji, C. Kim and D. A. Weitz, Shear thickening and scaling of the elastic modulus in a fractal colloidal system with attractive interactions, *Phys. Rev. E: Stat., Nonlinear, Soft Matter Phys.*, 2008, **77**(6), 8–11.
- 35 C. O. Osuji and D. A. Weitz, Highly anisotropic vorticity aligned structures in a shear thickening attractive colloidal system, *Soft Matter*, 2008, **4**(7), 1388–1392.
- 36 J. D. Park and K. H. Ahn, Structural evolution of colloidal gels at intermediate volume fraction under start-up of shear flow, *Soft Matter*, 2013, **9**(48), 11650–11662.
- 37 F. Radjai, J.-Y. Delenne, E. Azéma and S. Roux, Fabric evolution and accessible geometrical states in granular materials, *Granular Matter*, 2012, **14**(2), 259–264.
- 38 R. S. Rivlin, Further remarks on the stress–deformation relations for isotropic materials, *Journal of Rational Mechanics and Analysis*, 1955, **4**(5), 681–702.
- 39 M. Rotureau, J. Christophe Gimel, T. Nicolai and D. Durand, Monte Carlo simulation of particle aggregation and gelation: I. growth, structure and size distribution of the clusters, *Eur. Phys. J. E: Soft Matter Biol. Phys.*, 2004, **15**(2), 133–140.
- 40 P. H. S. Santos, O. H. Campanella and M. A. Carignano, Effective attractive range and viscoelasticity of colloidal gels, *Soft Matter*, 2013, **9**(3), 709.
- 41 M. Satake, Constitution of mechanics of granular materials through the graph theory, *Continuum Mechanical and Statistical Approaches in the Mechanics of Granular Materials*, 1978, pp. 47–62.
- 42 S. C. Schulz and W. Bauhofer, Shear influenced network dynamics and electrical conductivity recovery in carbon nanotube/epoxy suspensions, *Polymer*, 2010, **51**(23), 5500–5505.
- 43 K. C. Smith, Y.-M. Chiang and W. C. Carter, Maximizing Energetic Efficiency in Flow Batteries Utilizing Non-Newtonian Fluids, *J. Electrochem. Soc.*, 2014, **161**(4), A486–A496.
- 44 M. J. Stephen and J. P. Straley, Physics of liquid crystals, *Rev. Mod. Phys.*, 1974, **46**(4), 617.
- 45 J. Sun and S. Sundaresan, A constitutive model with microstructure evolution for flow of rate-independent granular materials, *J. Fluid Mech.*, 2011, **682**, 590–616.
- 46 V. Trappe, V. Prasad, L. Cipelletti, P. N. Segre and D. A. Weitz, Jamming phase diagram for attractive particles, *Nature*, 2001, **411**(6839), 772–775.
- 47 V. Trappe and D. A. Weitz, Scaling of the viscoelasticity of weakly attractive particles, *Phys. Rev. Lett.*, 2000, **85**(2), 449–452.
- 48 V. Trappe, E. Pitard, L. Ramos, A. Robert, H. Bissig and L. Cipelletti, Investigation of q-dependent dynamical heterogeneity in a colloidal gel by X-ray photon correlation spectroscopy, *Phys. Rev. E: Stat., Nonlinear, Soft Matter Phys.*, 2007, **76**(5), 051404.
- 49 J. Vermant and M. J. Solomon, Flow-induced structure in colloidal suspensions, *J. Phys.: Condens. Matter*, 2005, **17**(4), R187–R216.
- 50 M. Youssry, L. Madec, P. Soudan, M. Cerbelaud, D. Guyomard and B. Lestriez, Non-aqueous carbon black suspensions for lithium-based redox flow batteries: rheology and simultaneous rheo-electrical behavior, *Phys. Chem. Chem. Phys.*, 2013, **15**(34), 14476–14486.
- 51 X. Zhuang, A. K. Didwania and J. D. Goddard, Simulation of the quasi-static mechanics and scalar transport properties of ideal granular assemblages, *J. Comput. Phys.*, 1995, **121**(2), 331–346.

